PAPER

Check for updates

Optimization of SnO₂ electron transport layer for efficient planar perovskite solar cells with very low hysteresis†

Abed Alrhman Eliwi,‡[a] Mahdi Malekshahi Byranvand, [ID] ‡*[abcd] Paul Fassl, [ID] *[ab] Motiur Rahman Khan, [ID] [a] Ihteaz Muhaimeen Hossain,[ab] Markus Frericks, [ID] [ef] Simon Ternes,[ab] Tobias Abzieher,§[a] Jonas A. Schwenzer, [ID] [a] Thomas Mayer, [ID] [e] Jan P. Hofmann, [ID] [e] Bryce S. Richards, [ID] [ab] Uli Lemmer,[ab] Michael Saliba [ID] [cd] and Ulrich W. Paetzold [ID] *[ab]

Nanostructured tin oxide (SnO₂) is a very promising electron transport layer (ETL) for perovskite solar cells (PSCs) that allows low-temperature processing in the planar n–i–p architecture. However, minimizing current–voltage (*J–V*) hysteresis and optimizing charge extraction for PSCs in this architecture remains a challenge. In response to this, we study and optimize different types of single- and bilayer SnO₂ ETLs. Detailed characterization of the optoelectronic properties reveals that a bilayer ETL composed of lithium (Li)-doped compact SnO₂ (c(Li)-SnO₂) at the bottom and potassium-capped SnO₂ nanoparticle layers (NP-SnO₂) at the top enhances the electron extraction and charge transport properties of PSCs and reduces the degree of ion migration. This results in an improved PCE and a strongly reduced *J–V* hysteresis for PSCs with a bilayer c(Li)-NP-SnO₂ ETL as compared to reference PSCs with a single-layer or undoped bilayer ETL. The champion PSC with c(Li)-NP-SnO₂ ETL shows a high stabilized PCE of up to 18.5% compared to 15.7%, 12.5% and 16.3% for PSCs with c-SnO₂, c(Li)-SnO₂ and c-NP-SnO₂ as ETL, respectively.

Introduction

Perovskite solar cells (PSCs) have attracted enormous interest due to their rapid progress in power conversion efficiencies (PCEs) from 3.8%[1] to 25.5%.[2] To date, most PSCs with the highest PCEs are fabricated in the n–i–p structure, using a mesoporous TiO₂ layer as the electron transporting layer (ETL),[3–6] which, however, requires a high-temperature sintering process. In addition, PSCs employing TiO₂ ETLs are potentially unstable under ultraviolet (UV) illumination[7,8] and prolonged forward bias.[9] Therefore, many alternative n-type wide bandgap semiconductors – such as SnO₂, ZnO, WO₃, In₂O₃, Zn₂SnO₄, SrTiO₃, BaSnO₃, Ba₀.₈Sr₀.₂SnO₃ and Nb₂O₅ – have been studied as ETLs for the realization of high-performance, planar, and low-temperature-processed n–i–p PSCs.[10–12] SnO₂ has been identified as one of the most promising candidates owing to its favourable optoelectronic properties,[13,14] including low light absorption, appropriate energy level alignment with the perovskite, high electron mobility as well as low-temperature processing.[13–18]

However, planar PSCs employing 'standard' SnO₂ ETLs – without any additive or interface modification – often suffer from considerable current–voltage (*J–V*) hysteresis that limits the PCE of such devices.[15,18,19] One of the most accepted explanations for the appearance of hysteresis in PSCs is interface recombination in conjunction with ion migration[20–22] due to the existence of ionic defects (*e.g.*, vacancies, interstitials, antisites) in the perovskite crystal lattice.[23–27] Hysteresis in PSCs can be strongly suppressed by optimizing the energy level alignment, minimizing interfacial recombination, as well as

[a] *Light Technology Institute, Karlsruhe Institute of Technology, Engesserstrasse 13, 76131 Karlsruhe, Germany*

[b] *Institute of Microstructure Technology, Karlsruhe Institute of Technology, Hermann-von-Helmholtz-Platz 1, 76344 Eggenstein-Leopoldshafen, Germany. E-mail: paul.fassl@kit.edu, ulrich.paetzold@kit.edu*

[c] *Institute for Photovoltaics (IPV), University of Stuttgart, Stuttgart, Germany. E-mail: mahdi.malekshahi@ipv.uni-stuttgart.de*

[d] *IEK-5 Photovoltaik, Forschungszentrum Jülich, Jülich, Germany*

[e] *Surface Science Laboratory, Department of Materials and Earth Sciences, Technical University of Darmstadt, Otto-Berndt-Straße 3, 64287 Darmstadt, Germany*

[f] *InnovationLab GmbH, Speyerer Straße 4, 69115 Heidelberg, Germany*

† Electronic supplementary information (ESI) available. See DOI: 10.1039/d1ma00585e

‡ These authors contributed equally to this work.

§ Current address: National Renewable Energy Laboratory, 15013 Denver W Pkwy, Golden, CO 80401, USA.

optimizing the electron extraction efficiency and hole blocking properties.[19,21,28–32] Therefore, optimizing the electronic properties of the ETL/perovskite interface is one route for achieving hysteresis-free planar PSCs with highest PCEs. Many approaches have been proposed in this regard: (i) a bilayer ETL structure composed of two metal oxide films;[31–35] (ii) doping of the ETL;[5,18,19,36–40] (iii) an interfacial modification at the ETL/perovskite interface;[30,32,41–52] or (iv) doping the perovskite bulk.[53–56]

Lithium (Li) has been introduced as promising dopant[5,36,57–61] for improving the ETL/perovskite interface among others.[37–40] In case of mesoporous TiO_2, it has been shown that a post-treatment with Lithium bis(trifluoromethanesulfonyl)imide (Li-TFSI) as the Li source can improve the electronic properties of TiO_2, resulting in an enhanced electron mobility and a reduced electron trap density in TiO_2.[5,36,61] At the same time charge extraction from and energetic alignment with the perovskite are improved, thereby improving the PCE and reducing J–V hysteresis of PSCs.[5,36,61] In the case of SnO_2, Park et al.[60] added Li-TFSI directly into the $SnCl_2$ containing precursor solution and, more recently, Huang et al.[59] added LiCl into a colloidal SnO_2 nanoparticles (NPs) precursor solution. Both of these Li-doped SnO_2 films exhibited enhanced conductivity as well as improved the electron extraction from respectively electron injection into the perovskite layer, improving the PCE compared to reference PSCs. In addition to Li-doping, the use of potassium (K) at the ETL/perovskite interface has been demonstrated to strongly reduce the J–V hysteresis in n–i–p PSCs.[41,53,62,63] In that regard, Bu et al.[63] revealed that potassium hydroxide (KOH) is used as a stabilizer in a commercial SnO_2 NP dispersion (Alfa Aesar, tin(IV) oxide, 15% in H_2O colloidal dispersion, product number 44592). The authors proposed that K ions at the surface of SnO_2 react with the perovskite forming KBr by substitutional reaction.[63,64] The KBr-rich interface could passivate halide vacancies at the interface, resulting in high performance and hysteresis-free PSCs when employing this commercial product to form the SnO_2 ETL.[54–56,63]

Here, we study if the advantages of both Li and K can be exploited by introducing a bilayer ETL composed of Li-doped compact SnO_2 (c(Li)-SnO_2) and K-capped SnO_2 NPs (NP-SnO_2) layers, i.e. c(Li)-NP-SnO_2. The processing parameters such as concentrations of precursors and annealing temperature are optimized for PSCs employing compact SnO_2 (c-SnO_2) and c(Li)-SnO_2 single-layers as well as c-NP-SnO_2 and c(Li)-NP-SnO_2 bilayers as ETL. We investigate the surface chemistry of the various ETL configurations utilizing X-ray photoelectron spectroscopy (XPS), confirming the existence of Li and K at the surface of c(Li)-SnO_2 and c-NP-SnO_2/c(Li)-NP-SnO_2 ETLs, respectively. Photoluminescence (PL) spectroscopy and electrochemical impedance spectroscopy (EIS) indicate large improvements of electron extraction at the ETL/perovskite interface and charge transport across the perovskite layer together with a strong suppression of ion migration for c(Li)-NP-SnO_2 ETL. This results in a stabilized PCE of up to 18.5% with very low J–V hysteresis for PSCs employing c(Li)-NP-SnO_2 as ETL as compared to 15.7%, 12.5% and 16.3% for PSCs with c-SnO_2, c(Li)-SnO_2 and c-NP-SnO_2 as ETL, respectively.

Results and discussion

To investigate the effect of the various ETL configurations on the optoelectronic properties of the PSCs, we fabricated planar n–i–p PSCs with the layer stack (Fig. 1a–d): glass/indium tin oxide (ITO)/ETL/double-cation perovskite/2,2′,7,7′-tetrakis(N,N′-di-p-methoxy phenylamine)-9,9′-spirobifluorene (spiro-OMeTAD)/Au. First, we optimize the performance of PSCs employing the different ETL configurations – (a) c-SnO_2, (b) c-NP-SnO_2, (c) c(Li)-SnO_2, and (d) c(Li)-NP-SnO_2 – by tuning the thickness via the precursor solution concentrations as shown in Fig. S1–S4 in the ESI† (details can be found in the Experimental section). In addition, we optimize the annealing temperature after Li-TFSi treatment (Fig. S5, ESI†). The statistics of the photovoltaic parameters measured in reverse scan direction, for 15 devices (area: 0.078 cm^2) in each ETL configuration, are presented in Fig. 1e–h. The hysteresis index (HI) is calculated from the difference between the two J–V scan directions – defined as ($PCE_{reverse}$–$PCE_{forward}$)/$PCE_{reverse}$ – and a comparison of the HI is presented in Fig. 1i. The PSCs with c-SnO_2 ETL exhibit an average PCE and HI of 18.5% and 0.27, respectively. The PSCs with c-NP-SnO_2 ETL show a slightly lower average PCE of 18.3%, however, the HI is reduced to 0.06, which is attributed to the presence of K ions at the surface of the NP-SnO_2 layer (as will be verified later) that results in passivation of halide vacancies at the ETL/perovskite interface, in line with previous reports.[55,63] PSCs with c(Li)-SnO_2 ETL show the highest short-circuit current density (J_{SC}) and lowest open-circuit voltage (V_{OC}) among all ETLs, respectively,[65] however, the HI is strongly increased to 0.53. In contrast, PSCs with c(Li)-NP-SnO_2 ETL exhibit the combined benefits of Li and K with significant improvements in J_{SC} as well as FF as compared to PSCs with c-SnO_2 ETL, leading to an average PCE of 19.3% with by far the lowest HI of 0.03 among all studied ETLs.

Fig. 2a–d shows the champion J–V characteristics of PSCs with optimized ETLs for the different configurations. The difference between reverse and forward scan direction is shaded to highlight the degree of hysteresis. Devices with c(Li)-SnO_2, and c(Li)-NP-SnO_2 ETLs exhibit the highest J_{SC}, while the ones with c-NP-SnO_2 and c(Li)-NP-SnO_2 ETLs exhibit the highest FF together with very low J–V hysteresis. As a result of the combined improvement in J_{SC} and FF, PSCs with c(Li)-NP-SnO_2 exhibit the highest PCE of 20.4% in reverse scan direction compared to c-SnO_2, c-NP-SnO_2, and c(Li)-SnO_2, which exhibit champion PCEs of 19.5%, 19.3%, and 19.6%, respectively.

Stabilized PCEs (s-PCEs) are determined by maximum power point (MPP) tracking of the champion PSCs under continuous illumination for 300 s (Fig. 2e–h). s-PCEs of 15.7% and 12.5% are achieved for PSCs with c-SnO_2 and c(Li)-SnO_2 ETLs, respectively, which is much lower compared to the PCE from the reverse J–V scans (see Fig. 2a, c) due to the considerable J–V hysteresis. In contrast, PSCs with c-NP-SnO_2 and c(Li)-NP-SnO_2 ETLs with very low J–V hysteresis exhibit high s-PCEs of 16.3% and 18.5%, respectively. We note that the s-PCE in case of c-NP-SnO_2 and c(Li)-NP-SnO_2 is slightly lower than both the reverse and forward scan PCE. We speculate that this is related to a reduction in
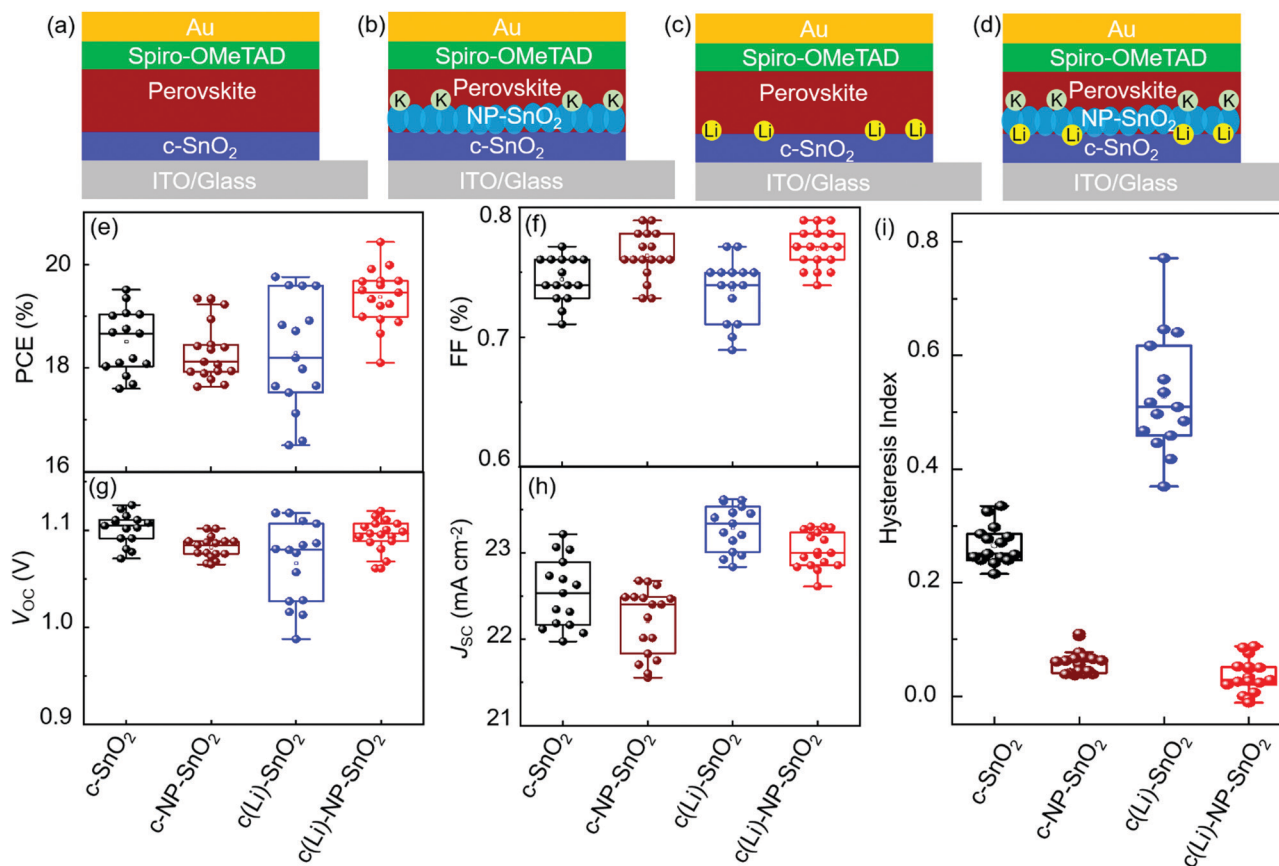
© 2022 The Author(s). Published by the Royal Society of Chemistry

Mater. Adv., 2022, **3**, 456–466 | **457**

Fig. 1 Schematic of the n–i–p PSC architecture employing (a) c-SnO$_2$, (b) c-NP-SnO$_2$ (c) c(Li)-SnO$_2$, and (d) c(Li)-NP-SnO$_2$ ETLs. Statistical photovoltaic parameters for 15 PSCs each employing the various ETL configurations in reverse scan direction: (e) PCE, (f) FF, (g) V_{OC}, (h) J_{SC}. (i) Statistical hysteresis index (HI) extracted from J–V curves.

charge carrier extraction during the first seconds of device operation, as recently reported by Thiesbrummel et al.[66] We also fabricated PSCs with a single SnO$_2$ NP layer (NP-SnO$_2$) as it is a well-established ETL in the literature[15–18,31,55,63,67,68] and our

laboratory.[69–71] The champion PSC with NP-SnO$_2$ ETL shows a reverse scan PCE and s-PCE of 19.3% and 16.3% respectively (Fig. S7, ESI†), which is much lower compared to the values achieved for the champion c(Li)-NP-SnO$_2$ ETL (Fig. 2d). Besides,
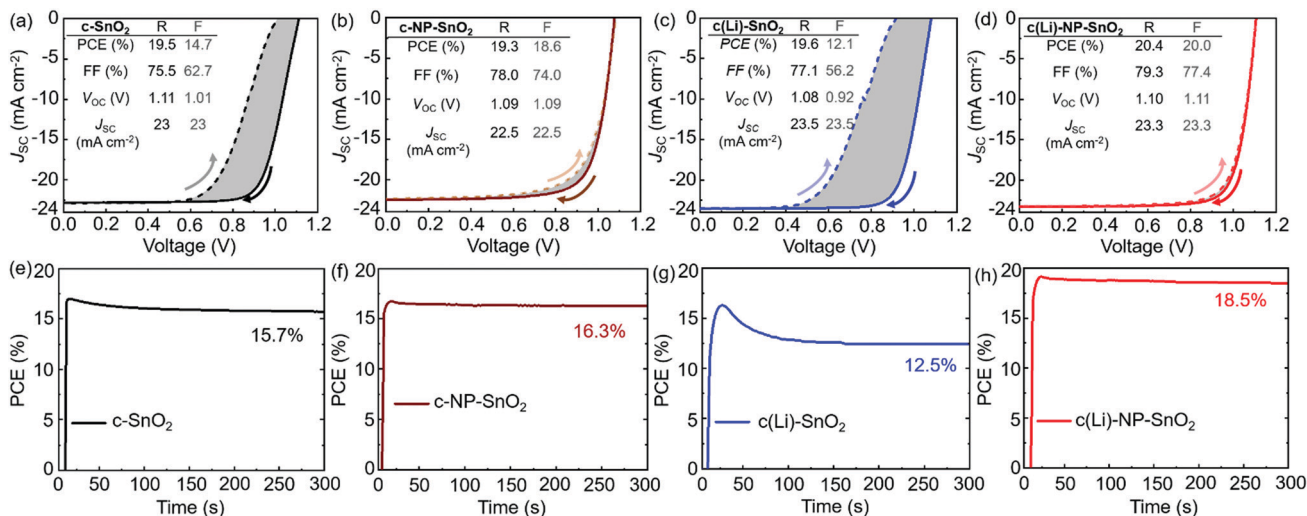

Fig. 2 Reverse (R) and forward (F) J–V scans and stabilized PCE (s-PCE) derived from MPP tracking of champion PSCs with (a and e) c-SnO$_2$, (b and f) c-NP-SnO$_2$, (c and g) c(Li)-SnO$_2$ and (d and h) c(Li)-NP-SnO$_2$ ETLs.

the PSCs with c(Li)-NP-SnO$_2$ ETL maintain a stable power output (>95% of the initial value) when measured under 1 Sun illumination for 24 h (Fig. S8, ESI†).

To identify the reasons for the differences in performance of PSCs employing the various ETL configurations, we firstly probe the ETL surface morphology by means of atomic force microscopy (AFM) and scanning electron microscopy (SEM). The AFM images depict that the morphology for the c-SnO$_2$ ETL (Fig. 3a) appears quite similar to that of ITO (Fig. S9a, ESI†), while the RMS roughness is slightly reduced from 2.9 nm to 2.2 nm. This observation is attributed to the existence of a thin and continuous SnO$_2$ compact layer on ITO. The c(Li)-SnO$_2$ ETL also exhibits a similar morphology and RMS roughness (2.1 nm) as compared the c-SnO$_2$ ETL without any observable aggregation of Li-TFSI salt (Fig. 3b). After deposition of SnO$_2$ NPs on top of the c-SnO$_2$ or c(Li)-SnO$_2$ layers, the film morphology slightly changes accompanied by a reduced RMS surface roughness of 1.3 nm and 1.4 nm, respectively, which is attributed to the formation of a smooth NP capping layer that homogenously covers the existing bumps of the underlying layers.[17,72]

Comparable morphology and RMS are also observed when SnO$_2$ NPs are deposited directly on bare ITO (Fig. S9b, ESI†). In addition, the SEM images demonstrate a similar surface morphology for the different ETL configurations in line with the results obtained by AFM (Fig. S10a–d, ESI†). The above observations are also in line with the comparable transmittance and reflectance spectra for the different ETLs (Fig. S11a and b, ESI†).

Furthermore, the transmission in the wavelength region ~450 nm is only slightly reduced as compared to bare ITO, resulting in a very low parasitic absorption of the respective PSCs.

Next, we examine if employing the different ETL configurations does alter the perovskite thin film morphology, thickness and crystallinity. SEM images in Fig. 3e–l and XRD spectra in Fig. S12 (ESI†) indicate that all perovskite thin films on the different ETLs exhibit a pin-hole free morphology with comparable grain size, thickness and XRD pattern. These findings confirm that the ETL sublayer has no significant effect on the perovskite film formation. The zoom-in of the cross-sectional SEM images of the of the ETLs/perovskite thin film interface indicates a similar thickness for the c-SnO$_2$ and c(Li)-SnO$_2$ ETLs, while that for c-NP-SnO$_2$ and c(Li)-NP-SnO$_2$ ETLs is slightly increased (Fig. 3i–l inset, highlighted in green). We note that we do not expect the c-SnO$_2$ layer (annealed at 200 °C) to be washed away or be redissolved by the water-based NP-SnO$_2$ depostion, in line with previous reports.[63]

Next, we investigate the surface chemistry of the various ETL configurations by means of X-ray photoelectron spectroscopy (XPS) to proof the presence of Li and/or K at the film surface and to study any potential effect on the chemical environment of SnO$_2$. Fig. 4a shows the survey spectra for the full accessible binding energy range, where the core level emissions were identified from reference values (see dotted lines and labels).[73] All four ETLs exhibit the expected lines related to tin (Sn) and oxygen (O). Furthermore, carbon (C) is present because
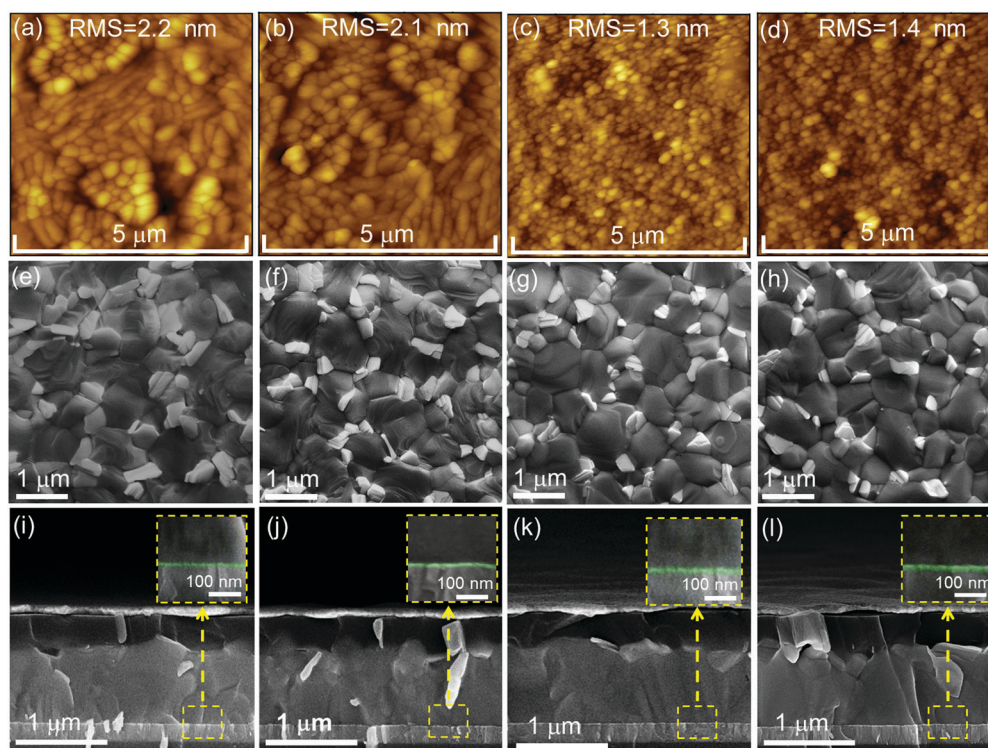

Fig. 3 AFM images of the surface morphology of (a) c-SnO$_2$, (b) c(Li)-SnO$_2$ (c) c-NP-SnO$_2$ and (d) c(Li)-NP-SnO$_2$ ETLs. Top and cross-sectional SEM images of perovskite thin films deposited on (e and i) c-SnO$_2$, (f and j) c(Li)-SnO$_2$, (g and k) c-NP-SnO$_2$ and (h and l) c(Li)-NP-SnO$_2$ ETLs.
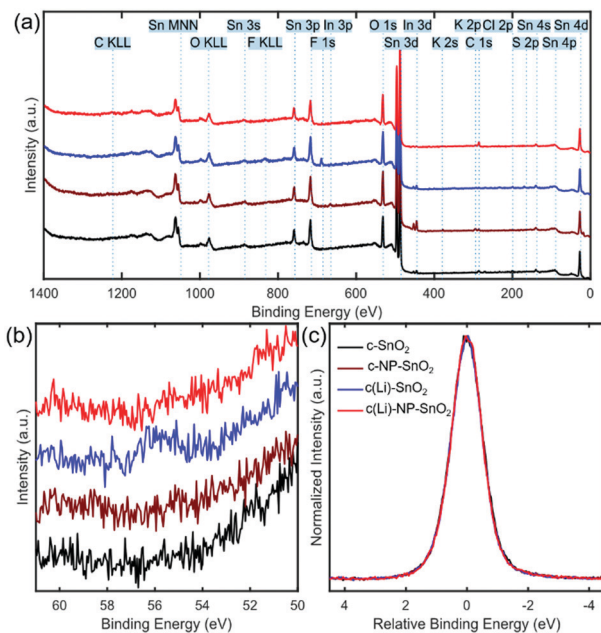
Fig. 4 (a) Survey spectra, (b) Li 1s emission, and (c) Sn $3d_{5/2}$ emission of the four different ETL configurations c-SnO$_2$, c-NP-SnO$_2$, c(Li)-SnO$_2$, and c(Li)-NP-SnO$_2$ measured by XPS. For shape comparison, the spectra in (c) were normalized and shifted.

of the *ex situ* preparation and sample transfer and handling in ambient air. For c-SnO$_2$ and c(Li)-SnO$_2$, a Cl 2p signal around 200 eV is detected, which is attributed to residuals of the SnCl$_2$ precursor (see Experimental section). In the case of c-NP-SnO$_2$ and c(Li)-NP-SnO$_2$, small potassium (K) peaks at ~294 eV (K 2p$_{3/2}$) and ~297 eV (K 2p$_{1/2}$) are detected (see Fig. S13, ESI†), which is attributed to residuals from KOH that is used for the synthesis of the NPs to stabilize the colloids as discussed above.[63]

Despite lithium having a relatively low photoionization cross-section,[74] *i.e.* it is barely detectable in the XPS survey spectrum, it can be unambiguously identified for the c(Li)-SnO$_2$ ETL from the Li 1s core level spectra at a binding energy of ~56 eV (Fig. 4b). This indicates that Li ions have been successfully doped into SnO$_2$. In addition, small peaks related to the fluorine F 1s and sulfur S 2p core levels at ~689 eV and ~170 eV originating from TFSI$^-$ anions at the film surface are detected in the survey spectrum (see Fig. 4a), in line with recent observations for Li-TFSI doped mesoporous TiO$_2$.[5] Critically, the signals of F, S, and Li disappear for the c(Li)-NP-SnO$_2$ ETL as their signal gets damped by the NPs. This reveals that there is no diffusion of the dopants from c(Li)-SnO$_2$ through the SnO$_2$ NPs towards the surface as otherwise the signal from the diffused dopant would be no longer be damped by the NPs and be still visible in the spectrum. The absence of a Li signal thereby shows that the Li-TFSI treatment affects only the interface between c-SnO$_2$ and NP-SnO$_2$. In Fig. 4c, we compare the normalized and shifted Sn $3d_{5/2}$ emission spectra for all different ETLs, which do not show any variations in the shape of the signal, indicating that the chemical environment of SnO$_2$ is the same for all four ETL configurations. We note, however,

that the Sn $3d_{5/2}$ emission is not very sensitive to chemical shifts;[75,76] thus, an influence of the Li-TFSI treatment might not be detectable. The comparable morphological and structural properties of the different ETLs and perovskite thin films on top mean that the difference in the photovoltaic performance must originate from changes in the optoelectronic properties at the ETL/perovskite interface. Therefore, we investigate the recombination behaviour and charge transfer kinetics between the perovskite and the different ETLs by means of photoluminescence quantum efficiency (Q_e^{lum}) and time resolved photoluminescence (TRPL).

The normalized steady state PL spectra of perovskite films deposited on the various ETL configurations measured in an integrating sphere exhibit a similar PL peak shape (Fig. S14, ESI†). This indicates that the perovskite bandgap and morphology are not strongly affected by the underlying ETL,[77] in line with the absorbance, SEM, AFM and XRD results. In order to determine the quasi-Fermi level splitting ($q \cdot \Delta E_F = V_{OC,rad} + k_B T \ln Q_e^{lum}$), we measure Q_e^{lum} of perovskite films deposited on ITO/ETL substrates at irradiation intensities comparable to 1 Sun illumination as a measure for the maximum obtainable V_{OC} (*i.e.*, the implied $V_{OC,imp} = \dfrac{\Delta E_F}{q}$) when employing this interface in a PSC.[78–80] As shown in Fig. 5a, a Q_e^{lum} of 5% (measured directly after turning on the laser) for perovskite films on a glass substrate relates to $V_{OC,imp}$ of ~1.13 V, while when deposited on the different ETL configurations Q_e^{lum} slightly reduces to ~1–2% which relates to $V_{OC,imp}$ in the range of ~1.1–1.12 V. The extracted values are comparable to the average (reverse scan) V_{OC} of the respective PSCs in the *J–V* characteristics (see Fig. 2), indicating that the V_{OC} is limited by the ETL/perovskite interface. We note that while the perovskite/HTL interface can also limit the V_{OC} substantially in certain device structures, as has been shown in several recent reports,[67,69,70,81,82] this interface is not the focus of this study and does not seem to result in a large additional interface recombination for our PSCs. Based on these results we can conclude that a reduction in interface recombination cannot explain the superior properties (enhanced J_{SC} and FF and lower hysteresis) of PSCs employing the c(Li)-NP-SnO$_2$ ETL, which is in line with the comparable reverse scan V_{OC} for the different ETLs.[82] For this reason, we measured the TRPL decay for ITO/ETL/ perovskite stacks to further analyze the charge extraction and non-radiative recombination properties (Fig. 5b). Despite the complicated interpretation of such transients,[83–86] at early times (*i.e.*, high initial charge carrier densities) the decay is affected by charge transfer to the ETL. At later times (*i.e.*, at low charge carrier densities), the decay is mainly governed by Shockley–Read–Hall (SRH) recombination at either the ETL/perovskite interface or within the bulk of the perovskite thin film and can be approximately described by a constant exponential slope.[79,85,86] Strikingly, the decay at early times (<100 ns) is much faster for the c(Li)-NP-SnO$_2$ ETL as compared to the other ETL configurations that all exhibit a very similar decay, indicating towards improved electron extraction capabilities of this specific ETL configuration.[15,85–87] One reason for that observation might be a lower amount of charge accumulation at this interface, which
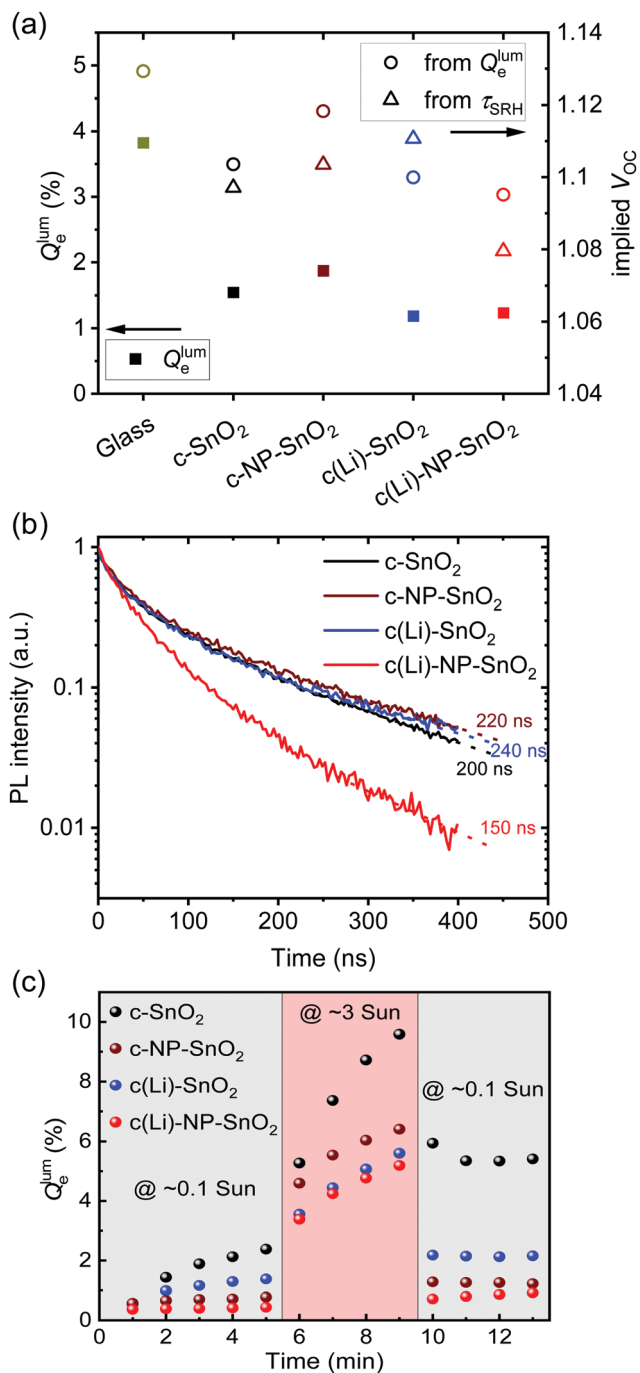
Fig. 5 (a) Left y-axis: External photoluminescence quantum efficiency (Q_e^{lum}) of perovskite films on glass and on ITO/ETL substrates for the different ETLs. Right y-axis: Implied V_{OC} calculated either via $V_{OC,imp} = V_{OC,rad} + \frac{kT}{q} \cdot \ln Q_e^{lum}$ or $V_{OC,imp} = \frac{kT}{q} \cdot \ln \frac{G_{ext}\Delta\tau_{SRH}}{n_0}$, (b) time resolved photoluminescence (TRPL) measurements of perovskite films on the various ITO/ETL configurations, (c) time dependent measurements of Q_e^{lum} at two different irradiation intensities of perovskite films on the various ITO/ETL configurations.

otherwise would quickly slow down the charge extraction process at early times.[83,85,86] A single exponential fit to the data at later times (~ 300 ns) allows estimating the SRH lifetime (τ_{SRH}) which is very similar for c-SnO$_2$, c-NP-SnO$_2$ and c(Li)-SnO$_2$ ETLs

($\tau_{SRH} \sim 220$ ns), while it is slightly lower for the c(Li)-NP-SnO$_2$ ETL ($\tau_{SRH} \sim 150$ ns). Assuming that τ_{SRH} is governed by recombination in the bulk of the perovskite films allows estimating $V_{OC,imp} = \frac{kT}{q}\ln\frac{G_{ext}\Delta\tau_{SRH}}{n_0}$, where G_{ext} is the charge carrier generation rate and n_0 is the thermal equilibrium concentration of electrons.[79,88]

The results of this analysis (average of 4 different spots) are included in Fig. 5a. While the values of $V_{OC,imp}$ for the c-SnO$_2$, c-NP-SnO$_2$ and c(Li)-NP-SnO$_2$ ETLs are slightly below that extracted from Q_e^{lum}, that for the c(Li)-SnO$_2$ ETL is slightly higher, which could indicate that the TRPL decay at later times is governed by additional processes for this ETL.

To explore the effect of ion migration and its effect on hysteresis for the various ETL configurations, we performed continuous light-soaking experiments at low (~ 0.1 Sun) and high (~ 3 Sun) irradiation intensity. This allows us to study the photo-brightening effect, which can be used to estimate the magnitude of ion migration and defect healing in a perovskite film (Fig. 5c).[56,89–93] In line with the measurements at 1 Sun intensity discussed above, the initial value of Q_e^{lum} at ~ 0.1 Sun is very similar ($\sim 0.5\%$) for all ETL configurations. However, Q_e^{lum} for c-SnO$_2$ as ETL exhibits fast rise dynamics even at these low irradiation intensities, while in contrast the photo-brightening effect is strongly suppressed in case of c(Li)-SnO$_2$, and almost completely suppressed for c-NP-SnO$_2$ and c(Li)-NP-SnO$_2$. Increasing the irradiation intensity to ~ 3 Sun where ion migration is expected to be strongly enhanced,[94,95] samples with c-NP-SnO$_2$, c(Li)-NP-SnO$_2$ and c(Li)-SnO$_2$ as ETL exhibit similar rise dynamics, while that for c-SnO$_2$ is again much stronger. Importantly, returning to the low intensity of ~ 0.1 Sun, c-NP-SnO$_2$, c(Li)-SnO$_2$ and c(Li)-NP-SnO$_2$ ETLs all exhibit a Q_e^{lum} that is around a factor ~ 1.6 higher compared to the value just before the high intensity step, while, in contrast, Q_e^{lum} for c-SnO$_2$ as ETL remains at a very high value of 5%, which is a factor ~ 2.5 higher. This reduced photo-brightening effect and suppressed hysteresis of Q_e^{lum}, when going from low-to-high-to-low intensities, indicates that ion migration is strongly suppressed when employing c-NP-SnO$_2$ and c(Li)-NP-SnO$_2$ as ETL and to some extent also for c(Li)-SnO$_2$.[56,68,89,90,93]

In summary, the Q_e^{lum} and TRPL results reveal that the degree of interface recombination at the ETL/perovskite interface is not strongly affected by the different ETL configurations, while there is an indication for a more efficient electron extraction in case of c(Li)-NP-SnO$_2$. In addition, ion migration seems to be strongly reduced for samples employing c-NP-SnO$_2$ and c(Li)-NP-SnO$_2$ as ETL with respect to the reference c-SnO$_2$ ETL. We hypothesize that the suppressed ion migration is related to a reduced charge accumulation at the ETL/perovskite interface and hence allows faster charge extraction, in line with the strongly reduced hysteresis in the respective PSCs.[92] It should be noted that from the results so far it is not completely clear why the hysteresis in c(Li)-SnO$_2$ is much higher as compared to c-NP-SnO$_2$ and c(Li)-NP-SnO$_2$.

Therefore, to further explore and understand the charge transport dynamics in PSCs with the various ETL configurations,
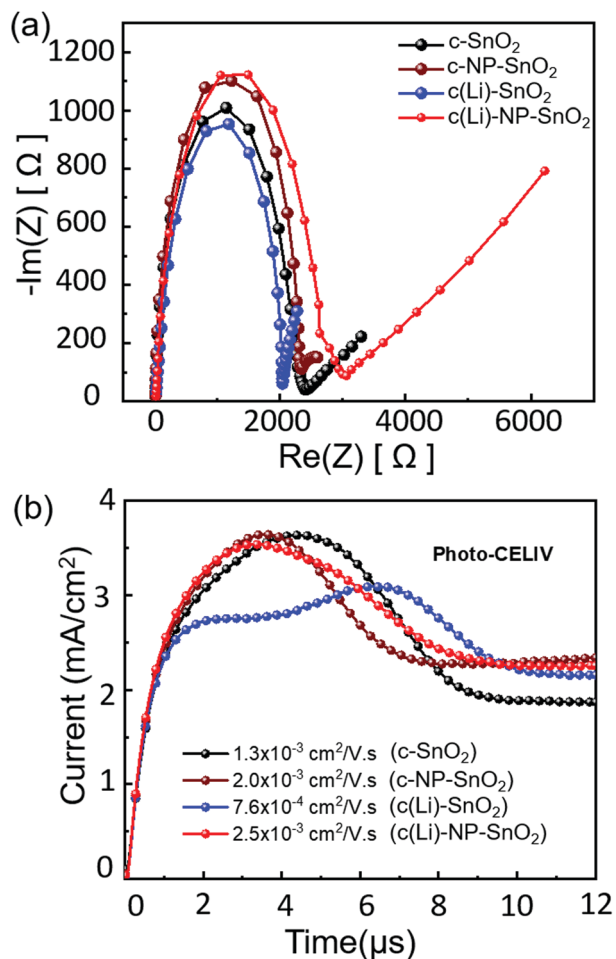
Fig. 6 (a) Electrochemical impedance spectroscopy (EIS) and (b) photo-generated charge extraction by linearly increasing voltage (photo-CELIV) measurements of PSCs with c-SnO$_2$, c(Li)-NP-SnO$_2$ and c(Li)-NP-SnO$_2$ ETLs.

we conduct electrochemical impedance spectroscopy (EIS) measurements to characterize the recombination behavior. The EIS measurements are performed under open-circuit conditions at 3 mW cm^{-2} intensity. The Nyquist plots of representative PSCs with the different ETL configurations feature two kinetically separated processes with clearly distinguishable semi-circles, recorded from 1 Hz to 1 MHz frequency (see Fig. 6a). As reported by Garcia-Belmonte *et al.* and others,[96–98] the semi-circle in the high frequency range (left side) represents the dielectric properties of the bulk of the perovskite film, and the semi-circle at low frequency range (right side) correlates to the recombination at the interface of the perovskite thin film and it's charge transport layers. The impedance response of PSCs is interpreted in terms of the equivalent circuit shown in Fig. S15 (ESI†) where R_s is the series resistance and C_b and R_1 refer to the capacitance and transport resistance of the bulk perovskite thin film, respectively. The chemical capacitance C_μ correlates to the charge accumulation at the interfaces of the perovskite and transport layers and the recombination resistance (R_{rec}) refers to the recombination resistance at the

interfaces.[33,99] The fitted parameters are summarized in Table S1 (ESI†). We observe that R_{rec} is highest in PSCs with c(Li)-NP-SnO$_2$ as ETL followed by c-NP-SnO$_2$, c-SnO$_2$ and c(Li)-SnO$_2$, reflecting the lowest recombination in PSCs with c(Li)-NP-SnO$_2$ as ETL compared to the others. Since the HTL remains identical for all PSCs, the change in R_{rec} is supposed to be originated from the ETL/perovskite interface. The value of C_μ suggests that charge accumulation at the ETL/perovskite interface decreases in the order c(Li)-SnO$_2$ > c-SnO$_2$ > c-NP-SnO$_2$ > c(Li)-NP-SnO$_2$. As mentioned previously, charge accumulation at the perovskite interfaces has been demonstrated to be one of the dominant reasons for J–V hysteresis.[20–22] The observed trend in charge accumulation behavior is consistent with the TRPL results and the fact that PSCs with c(Li)-NP-SnO$_2$ and c-NP-SnO$_2$ ETLs show the lowest hysteresis (Fig. 2d), while PSCs with c-SnO$_2$ and c(Li)-SnO$_2$ ETL show intermediate and maximum hysteresis, respectively (Fig. 2c and a). We note that this charge accumulation does not seem to affect the non-radiative recombination at the ETL/perovskite interface, as demonstrated by the similar value of Q_e^{lum}, and therefore the V_{OC}, but does affect the charge extraction properties and thereby the FF, J_{SC} and hysteresis.

Finally, to investigate whether charge transport throughout the perovskite absorber layer is also affected by the different ETL configurations and whether it correlates with the trend in device performance, we performed photogenerated charge extraction by linearly increasing voltage (photo-CELIV) measurements. Fig. 6b shows the typical photo-CELIV curves for all the PSCs with the peak position correlating to the mobility of the carriers (see details in the ESI†). This is because a peak position at later times indicates that a higher voltage is required for most efficient charge extraction.[100,101] Hence, for c(Li)-NP-SnO$_2$ and c-NP-SnO$_2$, comparatively lower voltages compared to c-SnO$_2$ and c(Li)-SnO$_2$ are required to extract all charge carriers, which we attribute to an enhanced charge accumulation in the latter, in line with the EIS results. In addition, an irregular double peak shape can be observed for c(Li)-SnO$_2$ ETL, with the total extracted charge carriers, as derived by integrating over the peak area in Fig. 6b, being strongly reduced compared to the other ETL configurations. The calculated mobilities for c(Li)-NP-SnO$_2$, c-NP-SnO$_2$, c-SnO$_2$ and c(Li)-SnO$_2$ are 2.5 × 10^{-3}, 2.0 × 10^{-3}, 1.3 × 10^{-3} and 7.6 × 10^{-4} cm^2 V^{-1} s^{-1}, respectively. Therefore, we have strong indication that the ETL configuration not only affects the charge extraction characteristics at the interface, but also improves the mobility within the perovskite film for PSCs with c(Li)-NP-SnO$_2$ as ETL as compared to c-SnO$_2$ and c(Li)-SnO$_2$.[102–105]

Conclusions

This work systematically investigates various single- and bilayer SnO$_2$ ETLs and the role of dopants and additives therein for use in highly-efficient planar n–i–p PSCs. SEM, XRD, and AFM results show that the different ETL configurations do not affect the perovskite film morphology and crystallinity. XPS data reveals that Li is successfully doped in the c(Li)-SnO$_2$ ETL and

that K is apparent in the ETLs formed using a commercial SnO_2 NPs colloidal solution. We introduce a novel bilayer c(Li)-NP-SnO_2 ETL that combines the advantages of Li and K, resulting in an improved charge extraction in conjunction with suppressed ion migration and reduced charge accumulation at the perovskite/ETL interface. The champion double-cation PSC with c(Li)-NP-SnO_2 ETL exhibits a remarkable PCE of 20.4% in the J–V scan and a stabilized PCE of around 18.5% after MPP tracking for 300 s. This is a result of a strongly reduced hysteresis and improvements in both FF and J_{SC} as compared to the other optimized ETL configurations. In summary, this work reports on an effective interface engineering approach for perovskite photovoltaics to improve their photovoltaic parameters.

Author contributions

A. A. E. and M. M. B. share equal contribution for conceiving the idea, developing the ETL optimization and processing of the perovskite solar cells. P. F. performed the photoluminescence quantum yield measurements and analysis. M. R. K. conducted the EIS and photo-CELIV characterizations and analysis, I. M. H. performed the TRPL measurements, which were analysed by P. F. M. F. performed the XPS measurements and analysis. S. T. and T. A. conducted the AFM and SEM measurement, respectively. J. A. S. developed the two-step perovskite deposition recipe. M. M. B., P. F. and U. W. P. drafted the manuscript. All co-authors discussed the paper and revised the manuscript. T. M., J. P. H., B. S. R., U. L. and, U. W. P. were involved in designing the experiments and supervised the work.

Conflicts of interest

The authors declare no conflict of interest.

Acknowledgements

References

1 A. Kojima, K. Teshima, Y. Shirai and T. Miyasaka, *J. Am. Chem. Soc.*, 2009, **131**, 6050–6051.

2 M. Green, E. Dunlop, J. Hohl-Ebinger, M. Yoshita, N. Kopidakis and X. Hao, *Prog. Photovoltaics*, 2021, **29**, 3–15.

3 J. Jeong, M. Kim, J. Seo, H. Lu, P. Ahlawat, A. Mishra, Y. Yang, M. A. Hope, F. T. Eickemeyer, M. Kim, Y. J. Yoon, I. W. Choi, B. P. Darwich, S. J. Choi, Y. Jo, J. H. Lee, B. Walker, S. M. Zakeeruddin, L. Emsley, U. Rothlisberger, A. Hagfeldt, D. S. Kim, M. Grätzel and J. Y. Kim, *Nature*, 2021, **592**, 381–385.

4 M. Jeong, I. W. Choi, E. M. Go, Y. Cho, M. Kim, B. Lee, S. Jeong, Y. Jo, H. W. Choi, J. Lee, J. Bae, S. K. Kwak, D. S. Kim and C. Yang, *Science*, 2020, **1620**, 1615–1620.

5 M. Kim, I. Choi, S. J. Choi, J. W. Song, S.-I. Mo, J.-H. An, Y. Jo, S. Ahn, S. K. Ahn, G.-H. Kim and D. S. Kim, *Joule*, 2021, **5**, 659–672.

6 Z. Saki, M. M. Byranvand, N. Taghavinia, M. Kedia and M. Saliba, *Energy Environ. Sci.*, DOI: 10.1039/D1EE02018H.

7 S.-W. Lee, S. Kim, S. Bae, K. Cho, T. Chung, L. E. Mundt, S. Lee, S. Park, H. Park, M. C. Schubert, S. W. Glunz, Y. Ko, Y. Jun, Y. Kang, H.-S. Lee and D. Kim, *Sci. Rep.*, 2016, **6**, 38150.

8 A. Farooq, I. M. Hossain, S. Moghadamzadeh, J. A. Schwenzer, T. Abzieher, B. S. Richards, E. Klampaftis and U. W. Paetzold, *ACS Appl. Mater. Interfaces*, 2018, **10**, 21985–21990.

9 H. J. Jung, D. Kim, S. Kim, J. Park, V. P. Dravid and B. Shin, *Adv. Mater.*, 2018, **30**, 1802769.

10 Z. Cao, C. Li, X. Deng, S. Wang, Y. Yuan, Y. Chen, Z. Wang, Y. Liu, L. Ding and F. Hao, *J. Mater. Chem. A*, 2020, **5**, 23566–23576.

11 Q. Xiong, L. Yang, Q. Zhou, T. Wu, C.-L. Mai, Z. Wang, S. Wu, X. Li and P. Gao, *ACS Appl. Mater. Interfaces*, 2020, **12**, 46306–46316.

12 L. Yang, Q. Xiong, Y. Li, P. Gao, B. Xu, H. Lin, X. Li and T. Miyasaka, *J. Mater. Chem. A*, 2021, **9**, 1574–1582.

13 Q. Jiang, X. Zhang and J. You, *Small*, 2018, **14**, 1801154.

14 E. H. Anaraki, A. Kermanpur, L. Steier, K. Domanski, T. Matsui, W. Tress, M. Saliba, A. Abate, M. Grätzel, A. Hagfeldt and J.-P. Correa-Baena, *Energy Environ. Sci.*, 2016, **9**, 3128–3134.

15 D. Yang, R. Yang, K. Wang, C. Wu, X. Zhu, J. Feng, X. Ren, G. Fang, S. Priya and S. Liu, *Nat. Commun.*, 2018, **9**, 3239.

16 Q. Jiang, L. Zhang, H. Wang, X. Yang, J. Meng, H. Liu, Z. Yin, J. Wu, X. Zhang and J. You, *Nat. Energy*, 2016, **2**, 16177.

17 A. J. Yun, J. Kim, T. Hwang and B. Park, *ACS Appl. Energy Mater.*, 2019, **2**, 3554–3560.

18 V. Rohnacher, F. Ullrich, H. Eggers, F. Schackmar, S. Hell, A. Salazar, C. Huck, G. Hernandez-Sosa, U. W. Paetzold, W. Jaegermann and A. Pucci, *Adv. Mater. Technol.*, 2020, 2000282.

19 S. Zhang, H. Si, W. Fan, M. Shi, M. Li, C. Xu, Z. Zhang, Q. Liao, A. Sattar, Z. Kang and Y. Zhang, *Angew. Chem., Int. Ed.*, 2020, **59**, 11573–11582.

20 T. Chen, Z. Sun, M. Liang and S. Xue, *Phys. Chem. Chem. Phys.*, 2020, **22**, 245–251.

21 S. A. L. Weber, I. M. Hermes, S.-H. Turren-Cruz, C. Gort, V. W. Bergmann, L. Gilson, A. Hagfeldt, M. Graetzel, W. Tress and R. Berger, *Energy Environ. Sci.*, 2018, **11**, 2404–2413.

22 D. Kang and N. Park, *Adv. Mater.*, 2019, **31**, 1805214.

23 T. Zhang, C. Hu and S. Yang, *Small Methods*, 2020, **4**, 1900552.

24 C. Eames, J. M. Frost, P. R. F. Barnes, B. C. O'Regan, A. Walsh and M. S. Islam, *Nat. Commun.*, 2015, **6**, 2–9.

25 M. M. Byranvand and M. Saliba, *Matter*, 2021, **4**, 1758–1759.

26 M. M. Byranvand and M. Saliba, *Sol. RRL*, 2021, **5**, 2100295.

27 J. Y. Ye, M. M. Byranvand, C. O. Martínez, R. L. Z. Hoye, M. Saliba and L. Polavarapu, *Angew. Chem.*, 2021, **133**, 21804–21828.

28 M. M. Byranvand, T. Kim, S. Song, G. Kang, S. U. Ryu and T. Park, *Adv. Energy Mater.*, 2018, **8**, 1702235.

29 M. F. Aygüler, A. G. Hufnagel, P. Rieder, M. Wussler, W. Jaegermann, T. Bein, V. Dyakonov, M. L. Petrus, A. Baumann and P. Docampo, *ACS Appl. Mater. Interfaces*, 2018, **10**, 11414–11419.

30 J. Jiménez-López, B. M. D. Puscher, D. M. Guldi and E. Palomares, *J. Am. Chem. Soc.*, 2020, **142**, 1236–1246.

31 P. Wang, R. Li, B. Chen, F. Hou, J. Zhang, Y. Zhao and X. Zhang, *Adv. Mater.*, 2020, **32**, 1905766.

32 L. Kegelmann, C. M. Wolff, C. Awino, F. Lang, E. L. Unger, L. Korte, T. Dittrich, D. Neher, B. Rech and S. Albrecht, *ACS Appl. Mater. Interfaces*, 2017, **9**, 17245–17255.

33 L. Lin, T. W. Jones, J. T. Wang, A. Cook, N. D. Pham, N. W. Duffy, B. Mihaylov, M. Grigore, K. F. Anderson, B. C. Duck, H. Wang, J. Pu, J. Li, B. Chi and G. J. Wilson, *Small*, 2020, **16**, 1901466.

34 H. B. Lee, N. Kumar, M. M. Ovhal, Y. J. Kim, Y. M. Song and J. J. Kang, *Adv. Funct. Mater.*, 2020, **30**, 2001559.

35 M. Hu, L. Zhang, S. She, J. Wu, X. Zhou, X. Li, D. Wang, J. Miao, G. Mi, H. Chen, Y. Tian, B. Xu and C. Cheng, *Sol. RRL*, 2020, **4**, 1900331.

36 F. Giordano, A. Abate, J. Pablo, C. Baena, M. Saliba, T. Matsui, S. H. Im, S. M. Zakeeruddin, M. K. Nazeeruddin, A. Hagfeldt and M. Graetzel, *Nat. Commun.*, 2016, **7**, 1–6.

37 R. Xue, X. Zhou, S. Peng, P. Xu, S. Wang, C. Xu, W. Zeng, Y. Xiong and D. Liang, *ACS Sustainable Chem. Eng.*, 2020, 0c01794.

38 Y. Bai, Y. Fang, Y. Deng, Q. Wang, J. Zhao, X. Zheng, Y. Zhang and J. Huang, *ChemSusChem*, 2016, **9**, 2686–2691.

39 J. Tian, J. Zhang, X. Li, B. Cheng, J. Yu and W. Ho, *Sol. RRL*, 2020, **4**, 2000090.

40 G. Yang, H. Lei, H. Tao, X. Zheng, J. Ma, Q. Liu, W. Ke, Z. Chen, L. Xiong, P. Qin, Z. Chen, M. Qin, X. Lu, Y. Yan and G. Fang, *Small*, 2017, **13**, 1601769.

41 N. Zhu, X. Qi, Y. Zhang, G. Liu, C. Wu, D. Wang, X. Guo, W. Luo, X. Li, H. Hu, Z. Chen, L. Xiao and B. Qu, *ACS Appl. Energy Mater.*, 2019, **2**, 3676–3682.

42 H. Li, Q. Wang, H. Li, J. Zhuang, H. Guo, X. Liu, H. Wang, R. Zheng and X. Gong, *J. Phys. Chem. C*, 2020, **124**, 12948–12955.

43 Y. Huang, S. Li, C. Wu, S. Wang, C. Wang and R. Ma, *New J. Chem.*, 2020, **44**, 8902–8909.

44 T. Cao, K. Chen, Q. Chen, Y. Zhou, N. Chen and Y. Li, *ACS Appl. Mater. Interfaces*, 2019, **11**, 33825–33834.

45 N. De Marco, H. Zhou, Q. Chen, P. Sun, Z. Liu, L. Meng, E. P. Yao, Y. Liu, A. Schiffer and Y. Yang, *Nano Lett.*, 2016, **16**, 1009–1016.

46 X. Liu, K. W. Tsai, Z. Zhu, Y. Sun, C. C. Chueh and A. K.-Y. Jen, *Adv. Mater. Interfaces*, 2016, **3**, 1600122.

47 W. Liu, Z. Ma, S. Wang, J. Jiang, N. Yuan and J. Ding, *J. Solid State Electrochem.*, 2018, **22**, 3751–3759.

48 J. Du, L. Feng, X. Guo, X. Huang, Z. Lin, J. Su, Z. Hu, J. Zhang, J. Chang and Y. Hao, *J. Power Sources*, 2020, **455**, 227974.

49 J. Yan, Z. Lin, Q. Cai, X. Wen and C. Mu, *ACS Appl. Energy Mater.*, 2020, **3**, 3504–3511.

50 M. Yu, L. Chen, G. Li, C. Xu, C. Luo, M. Wang, G. Wang, Y. Yao, L. Liao, S. Zhang and Q. Song, *RSC Adv.*, 2020, **10**, 19513–19520.

51 E. H. Jung, B. Chen, K. Bertens, M. Vafaie, S. Teale, A. Proppe, Y. Hou, T. Zhu, C. Zheng and E. H. Sargent, *ACS Energy Lett.*, 2020, **85**, 2796–2801.

52 X. Yu, X. Yan, J. Xiao, Z. Ku, J. Zhong, W. Li, F. Huang, Y. Peng and Y.-B. Cheng, *J. Chem. Phys.*, 2020, **153**, 014706.

53 D.-Y. Son, S.-G. Kim, J.-Y. Seo, S.-H. Lee, H. Shin, D. Lee and N.-G. Park, *J. Am. Chem. Soc.*, 2018, 7b10430.

54 F. Zheng, W. Chen, T. Bu, K. P. Ghiggino, F. Huang, Y. Cheng, P. Tapping, T. W. Kee, B. Jia and X. Wen, *Adv. Energy Mater.*, 2019, **9**, 1901016.

55 T. I. Alanazi, O. S. Game, J. A. Smith, R. C. Kilbride, C. Greenland, R. Jayaprakash, K. Georgiou, N. J. Terrill and D. G. Lidzey, *RSC Adv.*, 2020, **10**, 40341–40350.

56 M. Abdi-Jalebi, Z. Andaji-Garmaroudi, S. Cacovich, C. Stavrakas, B. Philippe, J. M. Richter, M. Alsari, E. P. Booker, E. M. Hutter, A. J. Pearson, S. Lilliu, T. J. Savenije, H. Rensmo, G. Divitini, C. Ducati, R. H. Friend and S. D. Stranks, *Nature*, 2018, **555**, 497–501.

57 Y. Qiang, Y. Xie, Y. Qi, P. Wei, H. Shi, C. Geng and H. Liu, *Sol. Energy*, 2020, **201**, 523–529.

58 Y. Wang, Y. Zhang, L. Zhang, Z. Wu, Q. Su, Q. Liu, Y. Fu, J. Li, Y. Li and D. He, *Mater. Chem. Phys.*, 2020, **254**, 123536.

59 Y. Huang, S. Li, C. Wu, S. Wang, C. Wang and R. Ma, *Chem. Phys. Lett.*, 2020, **745**, 137220.

60 M. Park, J.-Y. Kim, H. J. Son, C.-H. Lee, S. S. Jang and M. J. Ko, *Nano Energy*, 2016, **26**, 208–215.

61 J. H. Heo, M. S. You, M. H. Chang, W. Yin, T. K. Ahn, S.-J. Lee, S.-J. Sung, D. H. Kim and S. H. Im, *Nano Energy*, 2015, **15**, 530–539.

62 P. Zhu, S. Gu, X. Luo, Y. Gao, S. Li, J. Zhu and H. Tan, *Adv. Energy Mater.*, 2020, **10**, 1903083.

63 T. Bu, J. Li, F. Zheng, W. Chen, X. Wen, Z. Ku, Y. Peng, J. Zhong, Y.-B. Cheng and F. Huang, *Nat. Commun.*, 2018, **9**, 4609.

64 D. J. Kubicki, D. Prochowicz, A. Hofstetter, S. M. Zakeeruddin, M. Grätzel and L. Emsley, *J. Am. Chem. Soc.*, 2018, **140**, 7232–7238.

65 J. Zhang, R. Chen, Y. Wu, M. Shang, Z. Zeng, Y. Zhang, Y. Zhu and L. Han, *Adv. Energy Mater.*, 2018, **8**, 1701981.

66 J. Thiesbrummel, V. M. Le Corre, F. Peña-Camargo, L. Perdigón-Toro, F. Lang, F. Yang, M. Grischek, E. Gutierrez-Partida, J. Warby, M. D. Farrar, S. Mahesh, P. Caprioglio, S. Albrecht, D. Neher, H. J. Snaith and M. Stolterfoht, *Adv. Energy Mater.*, 2021, **11**, 2101447.

67 Q. Jiang, Y. Zhao, X. Zhang, X. Yang, Y. Chen, Z. Chu, Q. Ye, X. Li, Z. Yin and J. You, *Nat. Photonics*, 2019, **13**, 460–466.

68 S. G. Motti, D. Meggiolaro, A. J. Barker, E. Mosconi, C. A. R. Perini, J. M. Ball, M. Gandini, M. Kim, F. De Angelis and A. Petrozza, *Nat. Photonics*, 2019, **13**, 532–539.

69 S. Gharibzadeh, I. M. Hossain, P. Fassl, B. A. Nejand, T. Abzieher, M. Schultes, E. Ahlswede, P. Jackson, M. Powalla, S. Schäfer, M. Rienäcker, T. Wietler, R. Peibst, U. Lemmer, B. S. Richards and U. W. Paetzold, *Adv. Funct. Mater.*, 2020, **30**, 1909919.

70 S. Gharibzadeh, B. Abdollahi Nejand, M. Jakoby, T. Abzieher, D. Hauschild, S. Moghadamzadeh, J. A. Schwenzer, P. Brenner, R. Schmager, A. A. Haghighirad, L. Weinhardt, U. Lemmer, B. S. Richards, I. A. Howard and U. W. Paetzold, *Adv. Energy Mater.*, 2019, **9**, 1803699.

71 M. Malekshahi Byranvand, F. Behboodi-Sadabad, A. Alrhman Eliwi, V. Trouillet, A. Welle, S. Ternes, I. M. Hossain, M. R. Khan, J. A. Schwenzer, A. Farooq, B. S. Richards, J. Lahann and U. W. Paetzold, *J. Mater. Chem. A*, 2020, **8**, 20122–20132.

72 H. Yi, D. Wang, M. A. Mahmud, F. Haque, M. B. Upama, C. Xu, L. Duan and A. Uddin, *ACS Appl. Energy Mater.*, 2018, **1**, 6027–6039.

73 J. F. Moulder, W. F. Stickle, P. E. Sobol and K. D. Bomben, *Handbook of X-ray Photoelectron Spectroscopy: A Reference Book of Standard Spectra for Identification and Interpretation of XPS Data,* Physical Electronics, Inc., Minnesota, 1992.

74 J. H. Scofield, *J. Electron Spectrosc. Relat. Phenomena*, 1976, **8**, 129–137.

75 J. M. Themlin, R. Sporken, J. Darville, R. Caudano, J. M. Gilles and R. L. Johnson, *Phys. Rev. B*, 1990, **42**, 11914–11925.

76 J.-M. Themlin, M. Chtaïb, L. Henrard, P. Lambin, J. Darville and J.-M. Gilles, *Phys. Rev. B*, 1992, **46**, 2460–2466.

77 P. Fassl, V. Lami, F. J. Berger, L. M. Falk, J. Zaumseil, B. S. Richards, I. A. Howard, Y. Vaynzof and U. W. Paetzold, *Matter*, 2021, **4**, 1391–1412.

78 M. Stolterfoht, M. Grischek, P. Caprioglio, C. M. Wolff, E. Gutierrez-Partida, F. Peña-Camargo, D. Rothhardt, S. Zhang, M. Raoufi, J. Wolansky, M. Abdi-Jalebi, S. D. Stranks, S. Albrecht, T. Kirchartz and D. Neher, *Adv. Mater.*, 2020, **32**, 2000080.

79 T. Kirchartz, J. A. Márquez, M. Stolterfoht and T. Unold, *Adv. Energy Mater.*, 2020, **10**, 1904134.

80 L. Krückemeier, U. Rau, M. Stolterfoht and T. Kirchartz, *Adv. Energy Mater.*, 2020, **10**, 1902573.

81 J. J. Yoo, S. Wieghold, M. C. Sponseller, M. R. Chua, S. N. Bertram, N. T. P. Hartono, J. S. Tresback, E. C. Hansen, J.-P. Correa-Baena, V. Bulović, T. Buonassisi, S. S. Shin and M. G. Bawendi, *Energy Environ. Sci.*, 2019, **12**, 2192–2199.

82 M. Stolterfoht, P. Caprioglio, C. M. Wolff, J. A. Márquez, J. Nordmann, S. Zhang, D. Rothhardt, U. Hörmann, Y. Amir, A. Redinger, L. Kegelmann, F. Zu, S. Albrecht, N. Koch, T. Kirchartz, M. Saliba, T. Unold and D. Neher, *Energy Environ. Sci.*, 2019, **12**, 2778–2788.

83 J. Haddad, B. Krogmeier, B. Klingebiel, L. Krückemeier, S. Melhem, Z. Liu, J. Hüpkes, S. Mathur and T. Kirchartz, *Adv. Mater. Interfaces*, 2020, **7**, 2000366.

84 C. M. Wolff, P. Caprioglio, M. Stolterfoht and D. Neher, *Adv. Mater.*, 2019, **31**, 1902762.

85 B. Krogmeier, F. Staub, D. Grabowski, U. Rau and T. Kirchartz, *Sustainable Energy Fuels*, 2018, **2**, 1027–1034.

86 L. Krückemeier, B. Krogmeier, Z. Liu, U. Rau and T. Kirchartz, *Adv. Energy Mater.*, 2021, **11**, 2003489.

87 A. Al-Ashouri, E. Köhnen, B. Li, A. Magomedov, H. Hempel, P. Caprioglio, J. A. Márquez, A. B. Morales Vilches, E. Kasparavicius, J. A. Smith, N. Phung, D. Menzel, M. Grischek, L. Kegelmann, D. Skroblin, C. Gollwitzer, T. Malinauskas, M. Jošt, G. Matič, B. Rech, R. Schlatmann, M. Topič, L. Korte, A. Abate, B. Stannowski, D. Neher, M. Stolterfoht, T. Unold, V. Getautis and S. Albrecht, *Science*, 2020, **370**, 1300–1309.

88 D. Guo, V. M. Caselli, E. M. Hutter and T. J. Savenije, *ACS Energy Lett.*, 2019, **4**, 855–860.

89 Z. Andaji-Garmaroudi, M. Anaya, A. J. Pearson and S. D. Stranks, *Adv. Energy Mater.*, 2020, **10**, 1903109.

90 D. W. W. deQuilettes, W. Zhang, V. M. M. Burlakov, D. J. J. Graham, T. Leijtens, A. Osherov, V. Bulović, H. J. J. Snaith, D. S. S. Ginger and S. D. D. Stranks, *Nat. Commun.*, 2016, **7**, 11683.

91 S. Ghosh, S. K. Pal, K. J. Karki and T. Pullerits, *ACS Energy Lett.*, 2017, **2**, 2133–2139.

92 Y. Zhao, W. Zhou, W. Ma, S. Meng, H. Li, J. Wei, R. Fu, K. Liu, D. Yu and Q. Zhao, *ACS Energy Lett.*, 2016, **1**, 266–272.

93 E. Mosconi, D. Meggiolaro, H. J. Snaith, S. D. Stranks and F. De Angelis, *Energy Environ. Sci.*, 2016, **9**, 3180–3187.

94 Y.-C. Zhao, W.-K. Zhou, X. Zhou, K.-H. Liu, D.-P. Yu and Q. Zhao, *Light Sci. Appl.*, 2016, **6**, e16243.

95 G. Y. Kim, A. Senocrate, T. Yang, G. Gregori, M. Grätzel and J. Maier, *Nat. Mater.*, 2018, **17**, 445–450.

96 I. Zarazua, G. Han, P. P. Boix, S. Mhaisalkar, F. Fabregat-Santiago, I. Mora-Seró, J. Bisquert and G. Garcia-Belmonte, *J. Phys. Chem. Lett.*, 2016, **7**, 5105–5113.

97 B. Suarez, V. Gonzalez-Pedro, T. S. Ripolles, R. S. Sanchez, L. Otero and I. Mora-Sero, *J. Phys. Chem. Lett.*, 2014, **5**, 1628–1635.

98 Q. Wang, E. Mosconi, C. Wolff, J. Li, D. Neher, F. De Angelis, G. P. Suranna, R. Grisorio and A. Abate, *Adv. Energy Mater.*, 2019, **9**, 1900990.

99 T. Bu, X. Liu, Y. Zhou, J. Yi, X. Huang, L. Luo, J. Xiao, Z. Ku, Y. Peng, F. Huang, Y.-B. Cheng and J. Zhong, *Energy Environ. Sci.*, 2017, **10**, 2509–2515.

100 J. Peng, Y. Sun, Y. Chen, Y. Yao and Z. Liang, *ACS Energy Lett.*, 2016, **1**, 1000–1006.

101 N. Ahn, D. Y. Son, I. H. Jang, S. M. Kang, M. Choi and N. G. Park, *J. Am. Chem. Soc.*, 2015, **137**, 8696–8699.

102 Y. Chen, J. Peng, D. Su, X. Chen and Z. Liang, *ACS Appl. Mater. Interfaces*, 2015, **7**, 4471–4475.

103 M. Petrović, T. Maksudov, A. Panagiotopoulos, E. Serpetzoglou, I. Konidakis, M. M. Stylianakis, E. Stratakis and E. Kymakis, *Nanoscale Adv.*, 2019, **1**, 3107–3118.

104 C. Li, A. Wang, L. Xie, X. Deng, K. Liao, J. Yang, Y. Xiang and F. Hao, *J. Mater. Chem. C*, 2020, **8**, 3217–3225.

105 J. Peng, Y. Chen, K. Zheng, T. Pullerits and Z. Liang, *Chem. Soc. Rev.*, 2017, **46**, 5714–5729.